Strengthening Mechanisms in Nano Oxide Dispersion-Strengthened Fe-18Cr Ferritic Steel at Different Temperatures

RAJESH JARUGULA, SAMARTHA CHANNAGIRI, S. GANESH SUNDARA RAMAN, and G. SUNDARARAJAN

The objective of the present work is to evaluate isothermal uniaxial compressive deformation behavior of nano oxide dispersion-strengthened (n-ODS)-18Cr ferritic steel over a range of temperatures RT—1173 K and range of strain rates 10^{-4} to 10^{-2} s^{-1}. Irrespective of temperature, the influence of the strain rate on the yield strength is insignificant up to 673 K. It is found that the plot of variation of yield strength as a function of temperature exhibits three regimes, which indicates that different deformation mechanisms are governing the yield strength of n-ODS-18Cr steel. Transmission electron microscopic analysis of a sample deformed at the highest temperature of 1173 K and the lowest strain rate of 10^{-4} s^{-1} demonstrates no significant change in the grain size and nanoprecipitate size. Also, it confirms the interaction between dislocations and nanoprecipitates. Different deformation mechanisms governing the yield strength of n-ODS-18Cr steel are identified in all three regimes and their contributions are quantified.

I. INTRODUCTION

NANO oxide dispersion-strengthened (n-ODS) steels are being considered as candidate materials for nuclear fission and fusion reactors because of their attractive properties. These steels exhibit remarkable high temperature strength and resistance to irradiation due to the presence of nanoprecipitates (typically $Y_2Ti_2O_7$) of size ~ 2 to 5 nm.[1–9] In addition, these nanoprecipitates exert a Zener-like pinning force on the grain boundaries preventing the grain growth during consolidation and result in fine grain structure which enhances the strength due to Hall–Petch strengthening.[10,11] Most of the available literature on n-ODS steels are on n-ODS-9Cr and n-ODS-14Cr steels.[12–20] However, it is realized that the cladding tube material in generation IV fast breeder reactors must possess high corrosion and oxidation resistance.[21,22] These aspects persuade the researchers to synthesize the ODS steels with high Chromium (> 14 wt pct) and/or Aluminum (~ 4 to 5 wt pct) to improve the corrosion and oxidation resistance at high temperatures as high as 1473 K.[7,21–24]

Generally, n-ODS steels are produced by the powder metallurgy route. The processing of n-ODS steels involves several steps, namely mechanical alloying to disperse the yttria in the steel matrix followed by various consolidation processes to produce the final product. Mostly, hot isostatic pressing, spark plasma sintering, and hot extrusion processes are utilized.[18,25–29]

Earlier, several researchers reported that various strengthening mechanisms (such as lattice friction strengthening, solid solution strengthening, dislocation strengthening, grain boundary strengthening, and dispersion strengthening) contribute to the yield strength of n-ODS steels and their individual contribution to the yield strength was computed at room temperature.[18,30–36] It is interesting to note that the yield strength of n-ODS steels suddenly declined above the transition temperature (~ 773 K) probably due to activation of other deformation mechanisms caused by thermal activation. A few authors made an attempt on the modeling of yield strength above the transition temperature.[10,18,30,32,34] However, the assumptions and/or models considered by these authors may not be

RAJESH JARUGULA, and S. GANESH SUNDARA RAMAN are with the Materials Forming Laboratory, Department of Metallurgical and Materials Engineering, Indian Institute of Technology Madras, Chennai 600036, India. Contact e-mail: ganesh@iitm.ac.in SAMARTHA CHANNAGIRI is with the Advanced Facility for Microscopy and Microanalysis, Indian Institute of Science, Bangalore 560012, India. G. SUNDARARAJAN is with the Materials Forming Laboratory, Department of Metallurgical and Materials Engineering, Indian Institute of Technology Madras and also with the International Advanced Research Centre for Powder Metallurgy and New Materials, Hyderabad, 500005, India.

appropriate to predict the yield strength which further led to the overestimation of the results. For example, Nagini et al.[32] considered the Orowan strengthening mechanism at higher temperatures. However, it was noted that the extension of the Orowan mechanism to high temperatures was not successful because it considers only change in the temperature-dependent shear modulus. Moreover, transmission electron microscopic analysis of n-ODS steel deformed samples did not reveal Orowan bowing when the interaction between dislocations and nanoprecipitates was studied.[37–40] It was found that in n-ODS alloys, the model proposed by Rösler and Arzt[41] based on the dislocation detachment concept was appropriate to explain the interaction between dislocations and nanoparticles at high temperatures. Dade et al.[18] have not considered the grain boundary and dislocation strengthening mechanisms in modeling the yield strength above the transition temperature by assuming their contribution was insignificant at high temperatures. On the other hand, Schneibel et al.[10] reported that the materials having a stable fine grain structure exhibited high grain boundary strengthening (i.e., indirect strengthening) even at above homologous temperature of 0.5. Recently, Seils et al.[42] investigated the temperature-dependent strengthening contributions in austenitic and ferritic ODS steels from RT to 1073 K. These authors reported that above the transition temperature, deformation was possibly dominated by generation and annihilation of dislocations at grain boundaries. Based on these inferences, in the present work, the models which have taken the thermal activation into account are considered (discussed in detail in Section III–E–B).

The objective of the present work is to evaluate the compressive deformation behavior of n-ODS-18Cr steel over a wide range of temperatures RT—1173 K and range of strain rates 10^{-4} to 10^{-2} s^{-1}. It is identified that different deformation mechanisms are governing the yield strength of the present steel at different temperatures. Therefore, an effort has been made in the present work to assess the individual contribution of each mechanism to the yield strength at all the studied temperatures.

II. EXPERIMENTAL DETAILS

The material used in the present work i.e., n-ODS-18Cr ferritic steel was fabricated by the powder metallurgy route. Pre-alloyed powder of nominal composition Fe-18Cr-3W-0.3Ti (all in weight percentage) was produced by the gas atomization process in Ar atmosphere. The pre-alloyed powder was mixed with 0.35 wt pct yttria powder (of size 30 to 50 nm supplied by M/s Inframat Advanced Materials, LLC) and mechanically milled under Ar atmosphere for a duration of 6 hour in a stainless steel container attached to a high-energy horizontal attritor mill (supplied by M/s Zoz GmbH, Germany). No additional process control agents were added to the milling powders. The process temperature was maintained at room temperature by continuous supply of water to the grinding chamber.

For milling, a ball-to-powder ratio of 7.5:1 and rotation speed of 550 rpm was maintained. Post milling, the powder was filled in a mild steel can, then degassed at 723 K under 1×10^{-5} kPa of vacuum to remove adsorbed gases from milled powder and finally vacuum sealed. The sealed mild steel cans were upset forged at 1323 K in a 250 T hydraulic press. The upset forged billets were hot extruded at 1423 K with an extrusion ratio of 19. Finally, hot extruded rods were annealed at 1173 K for 1 hour and then quenched in water. The chemical composition of the extruded material was analyzed using inductively coupled plasma atomic emission spectroscopy (ICP-AES) (Model: Ultima-2CHR, Jobin—Yvon, France) and is listed in Table I. O and N analyzers (LECO, Model: TC436) and C analyzer (LECO, Model: CS444) were used to determine O, N, and C contents.

For compression testing, cylindrical samples with dimensions of 4 mm diameter and 6 mm height were machined from the hot extruded rods along a direction parallel to the extrusion direction. Isothermal uniaxial compression tests were carried out in air at different temperatures (RT, 473 K, 673 K, 773 K, 873 K, 973 K, 1073 K, and 1173 K) and at different strain rates (10^{-4}, 10^{-3}, and 10^{-2} s^{-1}). Because of the limited availability of the material, for each test condition only one test was carried out. Zwick/Roell Z100 universal testing machine was utilized to perform all the compression tests. The displacements were measured at the cross head. To minimize the friction between compression platens and the sample during deformation, a graphite lubricant was applied. For the tests carried out at higher temperatures, the samples were heated to the desired temperature at a heating rate of 10 K/min and then held at the test temperature for 15 minutes to homogenize the temperature across the sample prior to testing. After testing, the samples were allowed to cool down to room temperature in the furnace. From the load and displacement data, stress and strain values were calculated after subtracting the contribution from machine compliance.

Electron backscatter diffraction (EBSD) mapping was performed on the as-received sample using TSL software in an FEI Inspect F microscope operated at 20 kV. A step size of 50 nm was employed for EBSD scan. Prior to EBSD scan, the sample was ground on SiC emery papers up to 2500 grit size and then electrolytic polishing was performed in a Struers Lectropol machine operated at 20 V using an electrolyte consisting of 90 pct acetic acid and 10 pct perchloric acid.

Transmission electron microscopic (TEM) analysis was performed using FEI Tecnai G2 microscope attached with LaB$_6$ filament operated at 200 kV. For TEM investigation, discs from the as-received (hot extruded) and deformed samples were cut parallel to the extrusion direction and compression axis, respectively. These samples were mechanically thinned down to ~ 70 μm using SiC papers and the final thinning (to electron transparency) was carried out in Struers Tenupol twin-jet electrolytic polishing machine using an electrolyte consisting of 90 pct acetic acid and 10 pct perchloric acid.

Table I. Chemical Composition (Weight Percentage) of n-ODS-18Cr Ferritic Steel

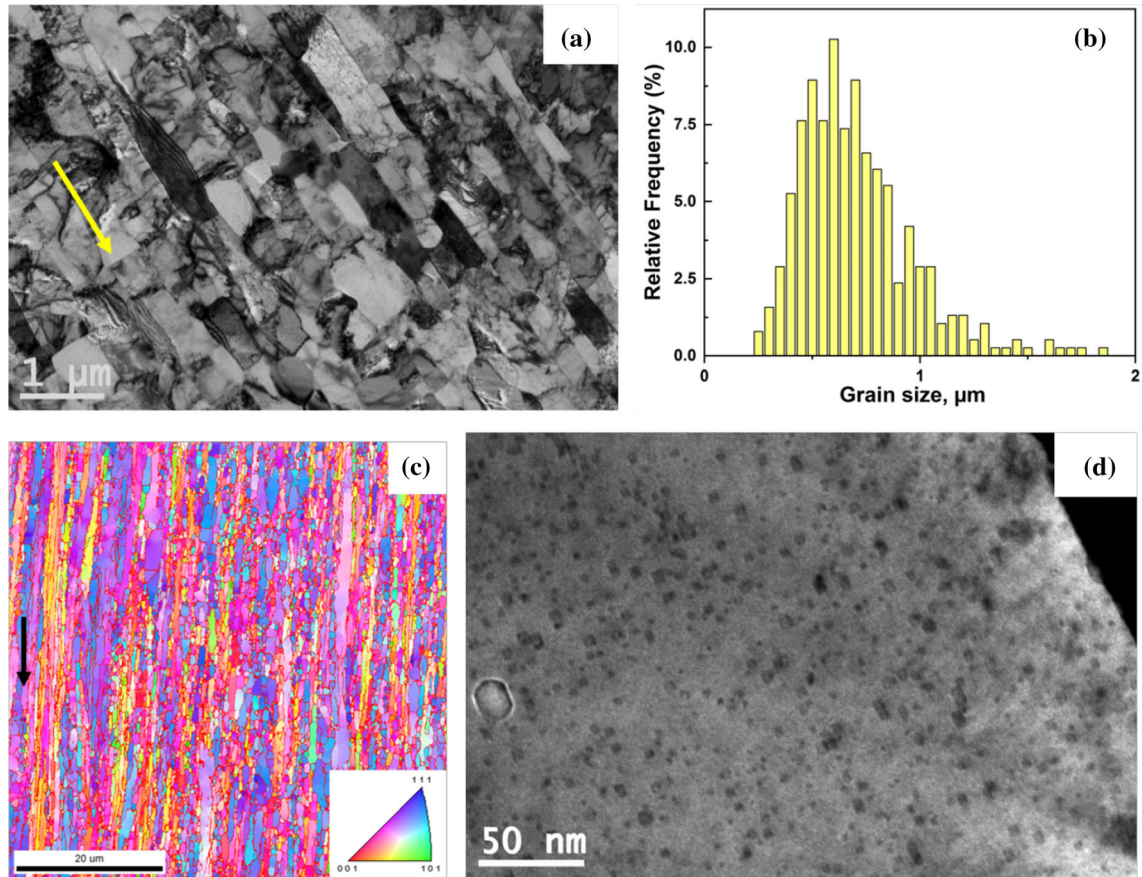| Fe	Cr	W	Ti	C	Total O	N	Y	Excess O
Balance	17.4	2.2	0.31	0.03	0.14	0.012	0.28	0.06

Fig. 1—(a) TEM bright-field (BF) micrograph of hot-extruded sample (arrow indicates extrusion direction), (b) grain size distribution, (c) Inverse pole figure map of hot-extruded rod, and (d) BF micrograph of nanoprecipitates in matrix.

III. RESULTS AND DISCUSSION

A. *Microstructure of Hot Extruded Material*

TEM bright-field micrograph and inverse pole figure map of the hot extruded sample in the longitudinal direction are shown in Figures 1(a) and (c). It exhibits an elongated grain structure in the extrusion direction. Grain size was measured by the linear intercept method (As per ASTM 112 standard) in TSL-orientation imaging microscopy (OIM) analysis software. Almost 80 pct (number fraction) grains exhibit a mean intercept length of 550 nm and remaining 20 pct grains have the size varying in the range 1.5 to 12 μm. Figure 1(b) depicts the grain size distribution histogram obtained based on the grain size measurement from TEM images (around 500 grains were measured) using the Image J software, which also indicates a similar average grain size. TEM bright-field image of nanoprecipitates distributed in the matrix is displayed in Figure 1(d). Small-angle X-ray scattering (SAXS) results indicate the average nanoprecipitate size of 4.1 nm and inter-particle spacing of 36 nm. More details regarding the microstructure of n-ODS-18Cr steel are given elsewhere.[39]

B. *Engineering Stress–Engineering Strain Curves*

The engineering stress–engineering strain curves for n-ODS-18Cr steel obtained from the experiments at different temperatures (RT, 473, 673, 773, 873, 973, 1073, and 1173 K) and at different strain rates (10^{-2}, 10^{-3}, and 10^{-4} s^{-1}) are presented in Figure 2. True stress–true strain curves (not shown here) generated from these curves indicated that the flow stress increases with increasing strain in all the samples up to 973 K irrespective of the strain rates. It can be inferred that the strain hardening (dislocation/dislocation interaction) is
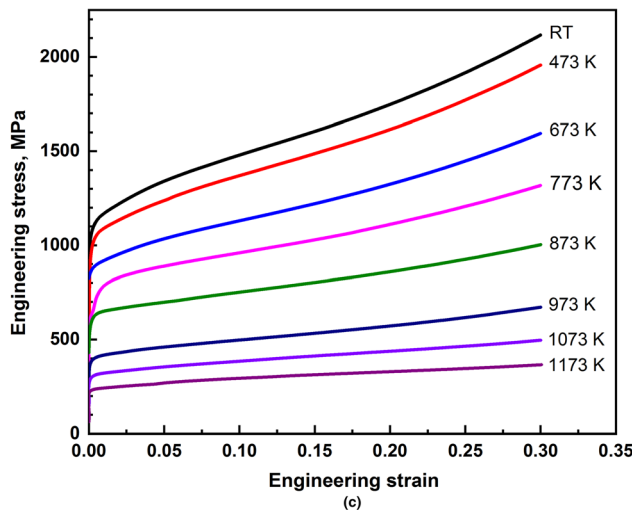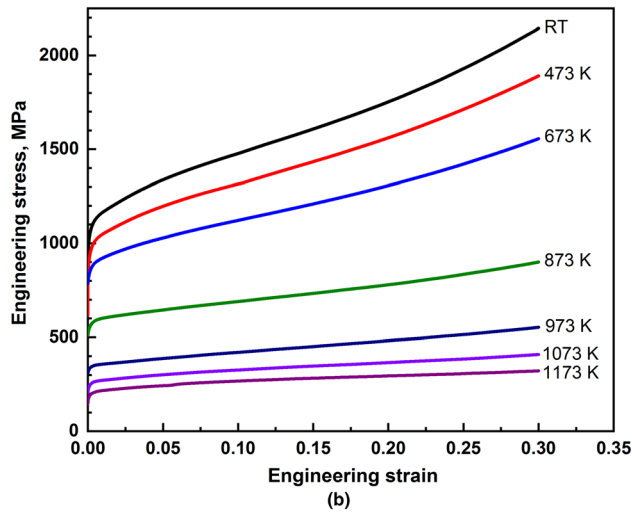
Fig. 3—Variation of yield strength with temperature at different strain rates.

stage followed by the dominance of flow softening process (dislocation annihilation) above the peak stress.

C. Deformation Behavior of n-ODS-18Cr Steel at RT to 1173 K

The variation of yield strength (found out with 0.2 pct offset strain) with temperature for different strain rates (10^{-2}, 10^{-3} and 10^{-4} s^{-1}) is presented in Figure 3. The data points have been joined by lines to give an idea about the trend. The yield strength gradually decreased with an increase in temperature up to 773 K and the influence of strain rate on the yield strength is not significant. However, above 773 K, a drastic decrease in yield strength is clearly evident with an increase in the temperature and a noticeable decrease in the yield strength with a decrease in the strain rate. The change of slope and the sudden drop in the yield strength above 773 K probably indicate a change in the deformation mechanism. In fact, three different regimes (RT to 773 K, 773 K to 973 K, and above 973 K) can be identified based on the slope in yield strength vs temperature curves (see Figure 3) indicating that different mechanisms might be governing the deformation in each regime.

D. Microstructure of Deformed Samples

TEM micrographs of samples deformed at 1073 K (10^{-2} s^{-1}) and 1173 K (10^{-4} s^{-1}) are shown in Figure 4. It can be seen from Figures 4(a) and (b) that the grain morphology changed from elongated to equiaxed and the change in nanoprecipitate size is insignificant in the sample after deformation at higher temperature (1173 K) and lower strain rate (10^{-4} s^{-1}). Dynamic restoration mechanisms would have played a role in change in grain morphology. A critical EBSD examination of samples is required in order to find out the exact restoration mechanism and it is beyond the scope of the present work. Majority of grains revealed substantial
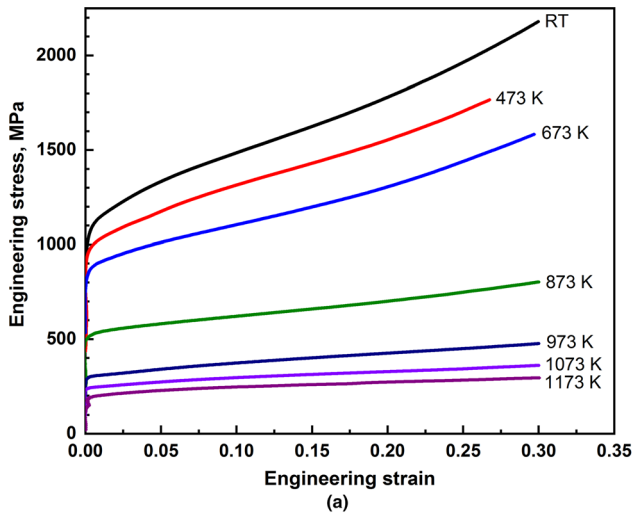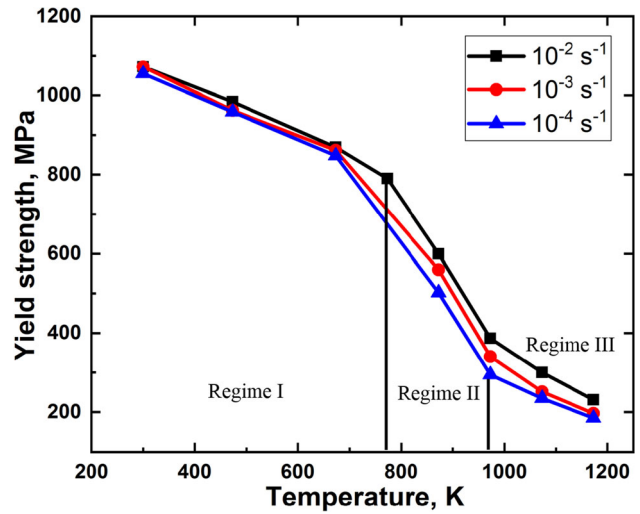
Fig. 2—Engineering stress—engineering strain curves obtained for n-ODS-18Cr steel at a range of temperatures (RT—1173 K) and different strain rates: (a) 10^{-4} s^{-1}, (b) 10^{-3} s^{-1}, and (c) 10^{-2} s^{-1}.

dominant in these samples. For the samples tested at all the strain rates, the flow curves obtained at and above 1073 K exhibit an initial dominance of strain hardening
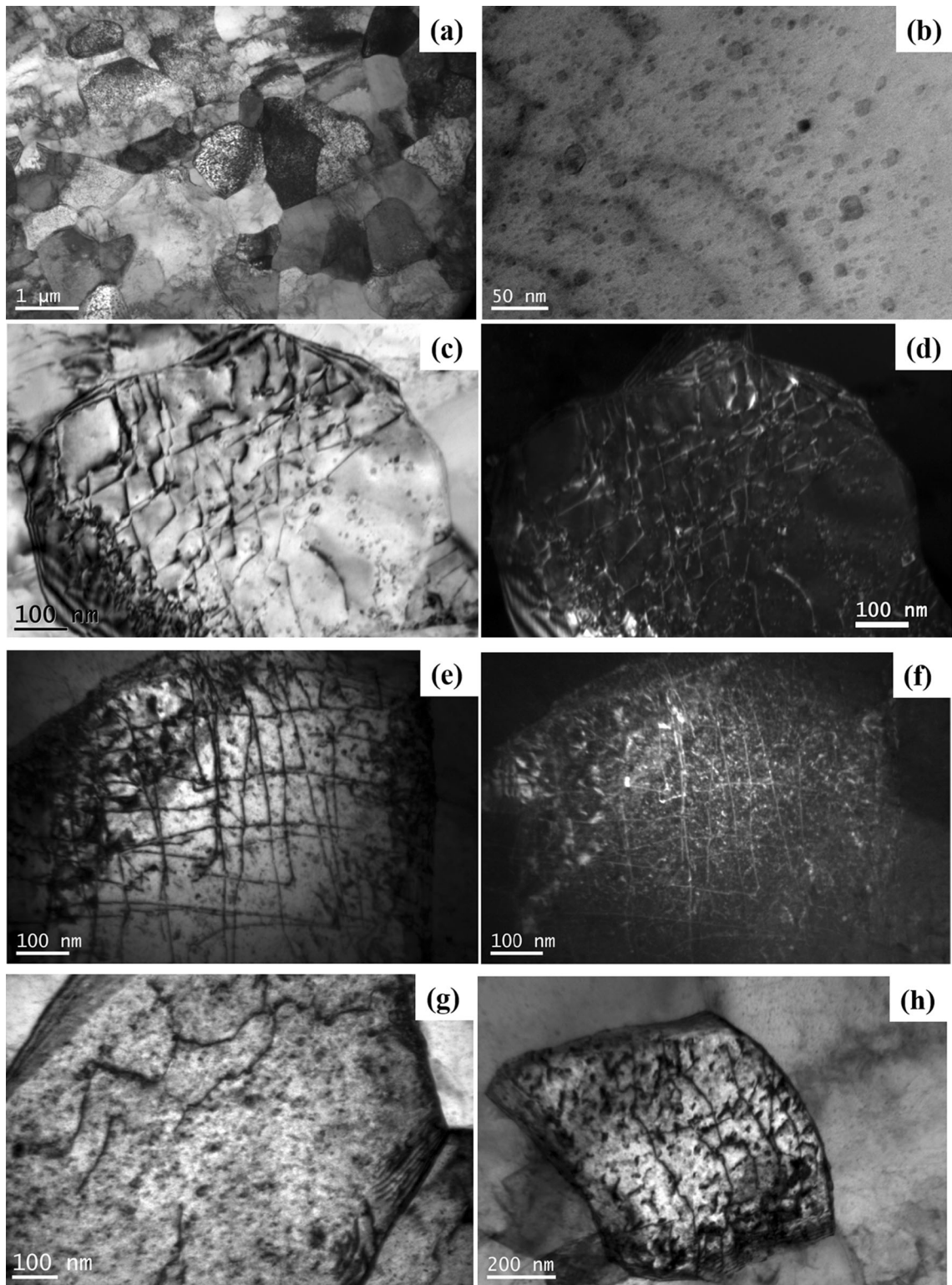
Fig. 4—(*a* and *b*) Bright-field (BF) micrographs displaying grain structure and nanoprecipitates in the matrix of a sample deformed at 1173 K and 10^{-4} s^{-1}, (*c, e, g,* and *h*) BF micrographs indicating particle/dislocation interaction in samples deformed at (c) 1073 K (10^{-2} s^{-1}) and (*e, g, h*) 1173 K (10^{-4} s^{-1}), (*d* and *f*) weak-beam dark-field micrographs taken in g.3g condition corresponding to (c) and (e).

dislocation activity after deformation (see Figure 4(a)). High-magnification TEM bright-field micrographs of samples deformed at 1073 K and 10^{-2} s^{-1} and 1173 K and 10^{-4} s^{-1} are presented in Figures 4(c), (e), (g), and

(h). The corresponding weak-beam dark-field micrographs for Figures 4(c) and (e) acquired in g.3g condition are presented in Figures 4(d) and (f), which confirm the interaction of dislocations with nanoprecipitates,

i.e., dislocations get pinned by the nanoprecipitates while traversing the slip plane. It suggests that nanoprecipitates are very effective in hindering the dislocation movement and contributing to the strength even at 1173 K and 10^{-4} s^{-1}.

E. Strengthening Mechanisms in n-ODS-18Cr Steel

The variation of yield strength (obtained at a range of temperatures from RT to 1473 K and a strain rate of 10^{-2} s^{-1}) normalized by temperature-dependent shear modulus (G_T (GPa) $= 89.5[1 - 0.84((T\text{-}300)/T_M)]$[43]) with temperature is presented as a master plot in Figure 5. The yield strength data in the temperature range from RT to 1173 K correspond to the hot extruded material (present study) and those in the temperature range from 1273 K to 1473 K correspond to the upset forged material (refer our earlier paper[44]). To get an overall insight of the deformation mechanisms governing the deformation in n-ODS-18Cr steel, the entire data are presented in the master plot. According to change in the slope, three different regimes (I, II, and III) can be identified in the master plot. The strengthening mechanisms contributing to strength in each regime are discussed below. The contribution of individual strengthening mechanism to strength is also quantified.

(i)   In regime I (RT to 773 K), the normalized yield strength is independent of temperature and thus represents the athermal strengthening regime.
(ii) In regimes II (773 K to 973 K) and III (973 K to 1473 K), the normalized yield strength decreases with increasing temperature indicating that multiple thermal activation mechanisms have started playing a substantial role resulting in the yield strength becoming lower than the athermal values. More interestingly, the strength obtained above 1273 K is mostly due to one dominant mechanism, *i.e.*, Rösler and Arzt mechanism[41]
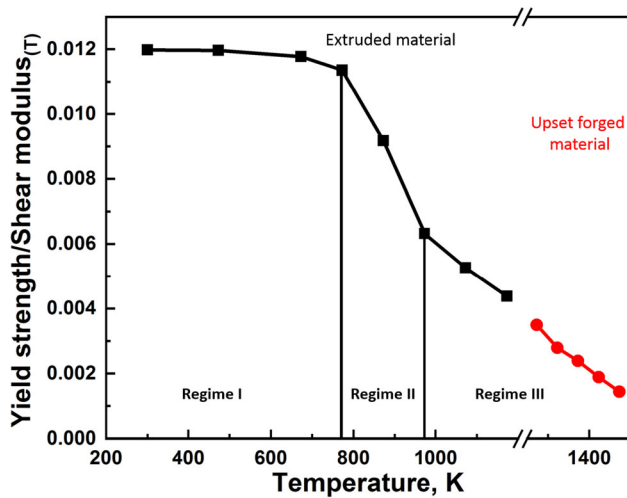

Fig. 5—Variation of yield strength (normalized by temperature-dependent shear modulus) with temperature at a strain rate of 10^{-2} s^{-1}.

(see Section III–E–B–B) and the contributions of other strengthening mechanisms are regarded as insignificant (more details are given in our earlier paper[44]).

1. Strengthening mechanisms in regime I

It has been already shown that the regime I represents athermal strengthening regime. It means that the decrease in strength with an increase in temperature only scales with the decrease in shear modulus with temperature.

It may be assumed that the following strengthening mechanisms are contributing to the strength of the material. They are

(i)   Lattice resistance to dislocation motion due to Peierls mechanism *i.e.*, friction stress (σ_f),
(ii)   Solid-solution strengthening (σ_{ss}),
(iii) Forest dislocation strengthening (σ_{dis}),
(iv)   Grain boundary strengthening (σ_{H-P}), and
(v)   Orowan strengthening (σ_{Or}).

a. Matrix strength In order to obtain the matrix strength for n-ODS-18Cr steel, uniaxial compression tests were carried out on Fe-18Cr-2W-0.3Ti steel without dispersoids [unpublished work]. After subtracting the grain size (13 μm) contribution from the yield strength of Fe-18Cr-2W-0.3Ti steel, the estimated matrix strength ($\sigma_M = \sigma_f + \sigma_{ss} + \sigma_{dis}$) at room temperature at a strain rate of 10^{-2} s^{-1} is 300 MPa. Above 873 K, to minimize the complexity of the problem regarding the fact that Hall–Petch constants are not available at high temperatures (*i.e.*, 873 K to 1173 K) for the present steel, yield strength (of Fe-18Cr-2W-0.3Ti steel) is assumed to be equal to the matrix strength (listed in Table II) of n-ODS-18Cr steel. Earlier, similar values of matrix strength for Fe-14Cr steel were also observed by Kim *et al.*[34]

The contribution of strengthening due to Peierls mechanism is considered to be negligible in the present work because of the following reasons. The magnitude of friction stress depends on different parameters *i.e.*, type of dislocation, slip system, and temperature. It is reported that the friction stress is close to zero when the screw dislocations overcome the Peierls barrier by kink-pair mechanism.[31,45] The strengthening due to Peierls mechanism need not be considered since this mechanism is important only at temperatures below 250 K.[46]

In the present work, the contribution of interstitial solid-solution strengthening is considered to be negligible due to the very small percentage of carbon (< 0.03wt pct). Moreover, the presence of Ti in these steels favors the formation of Ti(C, O) precipitates. However, the contribution of substitutional solid-solution strengthening to σ_{ss} is significant. Lacy and Gensamer[47] experimentally measured the effect of substitutional alloying elements in BCC iron and proposed a relation (Eq. [1]) based on the experiments.

$$\sigma_{ss} = 0.00689 k_s c^n, \qquad [1]$$

Table II. The Matrix Strength of Fe-18Cr-2W-0.3Ti Steel

Temperature, K	Matrix Strength, MPa
RT	300
873	155
973	88
1073	65
1173	40

where k_s is strengthening coefficient (1400 for Cr and 11000 for W), $n = 0.75$ for all elements, c is equilibrium concentration of substitutional elements in atomic percent. Accordingly, the contribution of Cr and W calculated separately, was 87 and 56 MPa, respectively.

Forest dislocation strengthening (σ_{dis}) is due to the dislocation/dislocation interaction and the contribution of σ_{dis} is estimated by Taylor equation[48] as

$$\sigma_{dis} = \alpha_d M G b \sqrt{\rho}, \qquad [2]$$

where α_d is a constant (1/3), M Taylor factor (3.06),[10] G shear modulus at room temperature = 89.5 GPa,[43] b is Burgers vector = 0.25 nm, and ρ is dislocation density. The contribution of forest dislocation strengthening at room temperature can be estimated by back calculation *i.e.*, $\sigma_{dis} = \sigma_M - \sigma_{ss} \approx 160$ MPa, which corresponds to a dislocation density of 5×10^{13} m^{-2}. The gradual decrease in yield strength in regime I due to decrease in temperature-dependent shear modulus (G_T (GPa) = $89.5[1 - 0.84((T\text{-}300)/T_M)])$[43]) is taken into account in Eq. [2] while calculating the dislocation strengthening. Mouawad *et al.*[49] reported that the dislocation density decreased to 1×10^{14} m^{-2} after spark plasma sintering at 1323 K compared to 3×10^{-14} m^{-2} after spark plasma sintering at a lower temperature of 1223 K. In another study, the dislocation density has been reported as 5×10^{14} m^{-2} after extrusion at 1123 K followed by warm rolling to 40 pct.[50] This value is one order of magnitude higher than that in the present work (estimated through back calculation). Considering the fact that hot extrusion was done at a relatively higher temperature of 1423 K in the present study, it can be said that the dislocation density (5×10^{13} m^{-2}) estimated in the present work is reasonable when compared with earlier reported values in literature.

b. Grain boundary strengthening Grain boundary strengthening is one of the major contributions to the strength in n-ODS steels due to the presence of fine grain structure. In the present work, the effect of aspect ratio of the grains on the Hall–Petch strengthening was not taken into account because the aspect ratio is not severe (*i.e.*, less than 3 (ASTM standard)) in the present steel. Moreover, the influence of elongated grain structure on the yield strength was insignificant in n-ODS-14Cr steel reported earlier.[20,51] It is estimated by Hall–Petch equation (Eq. [3]),[52] where the strength is inversely proportional to the square root of the average grain size.

$$\Delta\sigma_{H-P} = k_{H-P}\big/\sqrt{d} \qquad [3]$$

where k_{H-P} is Hall–Petch coefficient (MPa m$^{1/2}$) and d is grain diameter (m).

The average grain size of the present steel (= 550 nm) and k_{H-P} (= 0.338 MPa m$^{1/2}$) of n-ODS-14Cr steel reported by Kim *et al.*[34] are used in the present work to estimate the $\Delta\sigma_{H-P}$. Accordingly, the Hall–Petch contribution to the yield strength is 456 MPa. As per Figure 5, the gradual decrease in the yield strength in regime I is only due to the decrease of temperature-dependent shear modulus. So temperature-dependent shear modulus is incorporated in Eq. [3] and is expressed as Eq. [4].[53] Equation [4] is used to estimate the Hall–Petch contribution to the yield strength at remaining temperatures in regime I from 473 K to 773 K. For all temperatures, the Hall–Petch contribution to the yield strength is presented in Figure 6.

$$\Delta\sigma_{H-P}(T) = \sqrt{\frac{G_T}{G_{RT}}} \frac{k_{H-P}}{\sqrt{d}}, \qquad [4]$$

where G_{RT} is shear modulus at room temperature, temperature-dependent shear modulus, G_T (GPa) = $89.5[1 - 0.84((T\text{-}300)/T_M)]$.[43]

c. Orowan strengthening Orowan strengthening provides the major contribution to the strength in n-ODS steels. This is the classical mechanism proposed by Orowan for dislocations surmounting the impenetrable precipitates/dispersoids. An expression for the critical stress (*i.e.*, σ_{Or}) required for the dislocation to by-pass the dispersoids, as derived by Martin,[54] is provided in Eq. [5].

$$\sigma_{Or} = \frac{0.81 M G b}{2\pi\sqrt{1-v}(\lambda - 2r_s)} \ln\!\left(\frac{r_s}{b}\right), \qquad [5]$$

where M Taylor factor = 3.06,[10] temperature-dependent shear modulus G (GPa) = $89.5[1 - 0.84((T\text{-}300)/T_M)]$,[43] b Burgers vector = 0.25, v Poisson's ratio 0.29,[53] r_s[54] (= 0.816 r)—mean radius of intersection of a random plane with a spherical particle radius of r[39] (= 2.05 nm), λ[54] $\left(= \sqrt{\frac{2\pi}{3f}}r\right)$—inter-particle spacing from center to center = 36 nm. Using the above values, the Orowan dispersion strength (σ_{Or}) at room temperature (300 K) is obtained as 615 MPa. Orowan strengthening contribution to the yield strength for other temperatures in regime I (presented in Figure 6) is also estimated by considering the temperature-dependent shear modulus.

It is first assumed that the yield strength (σ_y) of the material can be estimated by a linear addition (LA) of contribution from different strengthening mechanisms as follows:

$$\sigma_{y,pre} = \sigma_M + \sigma_{H-P} + \sigma_{Or} \qquad [6]$$

The comparison of experimental yield strength and predicted yield strength (using Eq. [6]) for regime I is shown in Figure 6. The quantitative individual strengthening contribution (calculated by using the theoretical equations) to the total predicted yield strength is also
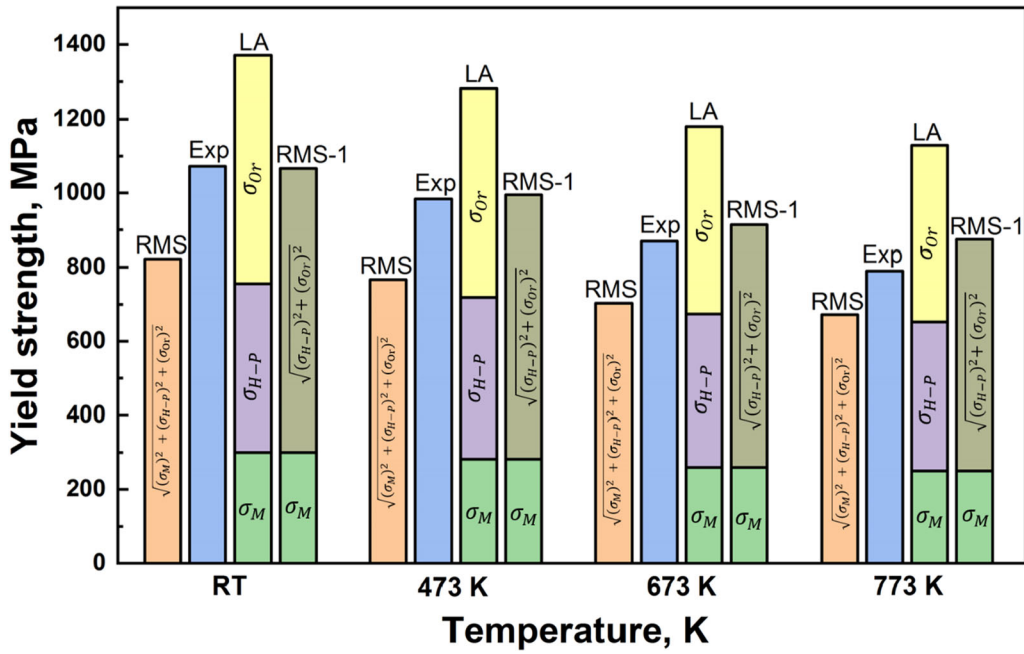
Fig. 6—Comparison of yield strength predicted using linear addition (LA) and root mean square (RMS) summation methods with experimental yield strength in regime I (RT to 773 K).

presented in Figure 6. It is noticed that the yield strength calculated using linear summation of individual strengthening mechanisms is much higher than the experimental yield strength. However, it is reported in the literature that when multiple strengthening mechanisms are contributing to the strength, a variety of superposition laws has been proposed depending on the strength and the density of obstacles present in a material.[55–58] These superposition laws cover the entire range from root mean square (RMS) to linear summation methods. Therefore, the yield strength is bounded in between the two limits as follows:

$$\sqrt{\sum_i \sigma_i^2} \leq \sigma_{0.2} \leq \sum_i \sigma_i, \qquad [7]$$

where i is the strengthening mechanism.

It can be seen that in regime I (Figure 6), when only grain boundary strengthening and Orowan strengthening (as they indicate identical strengths) were considered into RMS-1, i.e., (Eq. [9]), the predicted yield strength matches well with the experimental yield strength. Otherwise, experimental yield strength is limited within the bounds mentioned earlier.

$$\text{RMS-}\sigma_{y,\text{pre}} = \sqrt{\sigma_M^2 + \sigma_{H-P}^2 + \sigma_{Or}^2} \qquad [8]$$

$$\text{RMS-1-}\sigma_{y,\text{pre}} = \sigma_M + \sqrt{\sigma_{H-P}^2 + \sigma_{Or}^2} \qquad [9]$$

2. *Strengthening mechanisms in regimes II and III*

In these regimes, the use of temperature-dependent shear modulus in Hall–Petch and Orowan equations cannot explain such a sudden drop in the yield strength

above transition temperature (773 K) as it predicts a gradual decrease in strength. Thermally activated mechanisms might be playing a crucial role in these regimes. For example, Table II clearly shows a drastic reduction in the matrix strength with an increase in temperature indicating that thermally activated mechanisms might be governing the deformation behavior. Schneibel et al.[10] considered three models to describe the temperature dependence of the strength in n-ODS-14Cr steel, in which diffusional creep model (Coble creep) and thermally activated absorption of dislocations at grain boundaries (model due to Carlton and Ferreira[59]) exhibit a much steeper fall in the strength than the original behavior at transition temperature. Moreover, the transition temperature decreases with decreasing grain size which results in the intersection of curves obtained for different grain sizes. Above transition temperature, the strength predicted by Coble creep model reduces too strong and quickly approaches zero. In n-ODS steels, it has been reported that the presence of nanoprecipitates as well as segregation of Cr and W at grain boundaries inhibit Fe self-diffusion, which restrict the diffusion creep.[11] Therefore, these models are insufficient to describe the sudden decline in strength. In contrast, Blum and Zeng model[60,61] (which considers steady-state deformation involved in fine grained materials due to the balancing between generation and annihilation of dislocations at grain boundaries) predicts the strength dependence on temperature more appropriately. However, these authors did not calculate the Orowan strengthening contribution to the yield strength at high temperature. In fact, these authors obtained alloy strength (matrix + Orowan strength) for an ODS steel where grain boundary strengthening is negligible. In case of Orowan strengthening contribution at high temperatures, the extension of the Orowan

mechanism to high temperatures was not successful. In Orowan equation, only shear modulus parameter depends on the temperature and when only this change is taken into account it results in the overestimation of the results. Kim et al.[62] studied the deformation behavior of n-ODS-14Cr steel by performing stress relaxation experiments and reported that the dislocation climb mechanism was governing the deformation in the temperature range of 873 K to 1073 K. However, the same authors reported that dislocation climb mechanism alone cannot explain the high stress exponents or threshold stress.[34] Earlier, Srolovitz et al.[63] found that there is an attractive interaction existing between dislocations and incoherent particles due to relaxation of the strain field at matrix/particle interface because of slipping and diffusion leading to a threshold stress. Based on this concept, Arzt et al.[41,64,65] proposed a model which considers the thermally activated dislocation overcoming the particle by dislocation detachment mechanism. Based on the above inferences, in the present work, in order to model the decrease in yield strength with an increase in temperature in regimes II and III, the models which have taken thermal activation into account i.e., Blum and Zeng model and Rösler and Arzt model are considered and are discussed below.

a. Blum and Zeng model Blum and Zeng proposed a model for decrease of strength with an increase in temperature in case of ultrafine grained (ufg) materials.[60,61,66,67] The model considers the steady-state deformation mechanism attained in ufg materials resulting from the balance between the dislocation generation and annihilation at high-angle grain boundaries. This model considers the thermally activated absorption of dislocations at grain boundaries, which explains the decrease in strength at high temperatures. In ODS steels, although the extent of reduction in k_{H-P} decreases with an increase in temperature, considerable strength dependence on grain size (i.e., Hall–Petch coefficient) is observed even above the transition temperature where sudden decline in yield strength is observed. Irrespective of fine grained structure and the absence of subgrains, for a given stress corresponding to a constant steady-state dislocation density, for a given strain rate, fine grains require to accommodate higher density of dislocations to be stored in order to attain the same dislocation spacing at the grain boundaries. The presence of higher density of dislocations in small grains results in high flow stress. This model explains how the grain boundaries strengthen and/or soften the material in different regimes by enhancing the rate at which the dislocations are stored and/or annihilated at the grain boundaries. For detailed discussion and derivation of the model, the reader is referred to the paper by Blum and Zeng.[60,61] The variation of stress as a function of temperature and strain rate is predicted by Blum–Zeng model using Eq. [10].

$$\sigma_{B-Z} = G\left(\frac{\pi(1-v)M^9}{1.2^4}\right)^{\frac{1}{8}}\alpha\left(\frac{1-c+c^3}{c^3}\right)^{\frac{1}{2}}\left(\frac{k_B T\dot{\varepsilon}}{GbD_b}\right)^{\frac{1}{8}}\left(\frac{d}{b}\right)^{-\frac{1}{2}}$$

[10]

where temperature-dependent shear modulus, G (GPa) $= 89.5[1 - 0.84((T-300)/T_M)]$,[43] v is the Poisson's ratio $= 0.29$,[53] M is the Taylor factor $= 3.06$,[10] α is the dislocation interaction constant for dislocations inside the grains $= 0.3$,[60] c is a constant assumed to be 0.5 in Blum and Zeng,[61] k_B is the Boltzmann constant, T is the absolute temperature (K), $\dot{\varepsilon}$ is the strain rate (s^{-1}), b is the Burgers vector $= 0.25$ nm, D_b is the grain boundary diffusion coefficient. The temperature dependence of $\delta_b D_b \left(= \delta_b D_{b0}\exp\left(-Q_{gb}/RT\right)\right)$ was calculated by taking $\delta_b D_{b0} = 1.1 \times 10^{-12}$ m^3/s and activation energy for grain boundary diffusion of α-iron $Q_{gb} = 174$ kJ/mol,[68] δ_b is the grain boundary width assumed to be equal to Burgers vector and d is the grain size $= 550$ nm.

Using these values, the strength (σ_{B-Z}) due to grain boundaries above transition temperature is estimated from Eq. [10] and presented in Figure 7.

b. Rösler and Arzt mechanism (dislocation detachment (DD) model) Arzt and coworkers proposed a new model to describe the high-temperature deformation behavior of ODS alloys, which considers the thermally activated dislocations surmounting the particles by dislocation detachment mechanism.[41,64,65] The thermally activated dislocation is attracted to particle's arrival side due to the relaxation at matrix/particle interface caused by diffusion. Then the dislocation climbs down the particle and is pinned at the departure side. In order to detach the dislocation from the particle, sufficient thermal energy and/or stress has to be supplied and it is a rate controlling step in the ODS alloys. For more details about the model, the readers are referred to the paper by Rösler and Arzt.[41] According to the DD model, the variation in strain rate as a function of stress and temperature is given by Eq. [11]. In the present study, compression tests were carried out at constant strain rate and stress was calculated. Therefore, it is useful to recast Eq. [11] to predict the stress as a function of temperature and strain rate. Eq. [12] recast in such a manner is given below.

$$\dot{\varepsilon} = \dot{\varepsilon}_o \exp\left(-\frac{Gb^2r\left[(1-K_r)\left(1-\frac{\sigma_{DD}}{\sigma_d}\right)\right]^{3/2}}{k_B T}\right)$$

[11]

$$\sigma_{DD} = \sigma_d\left(1 - \left(\left(\frac{1}{1-K_r}\right)\left[\ln\left(\frac{\dot{\varepsilon}}{\dot{\varepsilon}_o}\right)\left(-\frac{k_B T}{Gb^2r}\right)\right]^{2/3}\right)\right)$$

[12]

$$\sigma_d = \sigma_{Or}\sqrt{1 - K_r^2}$$

[13]

$$\dot{\varepsilon}_o = \frac{3\lambda\rho D_v}{b}$$

[14]

In Eqs. ([11] through [14]), temperature-dependent shear modulus, G (GPa) $= 89.5[1 - 0.84((T-300)/$
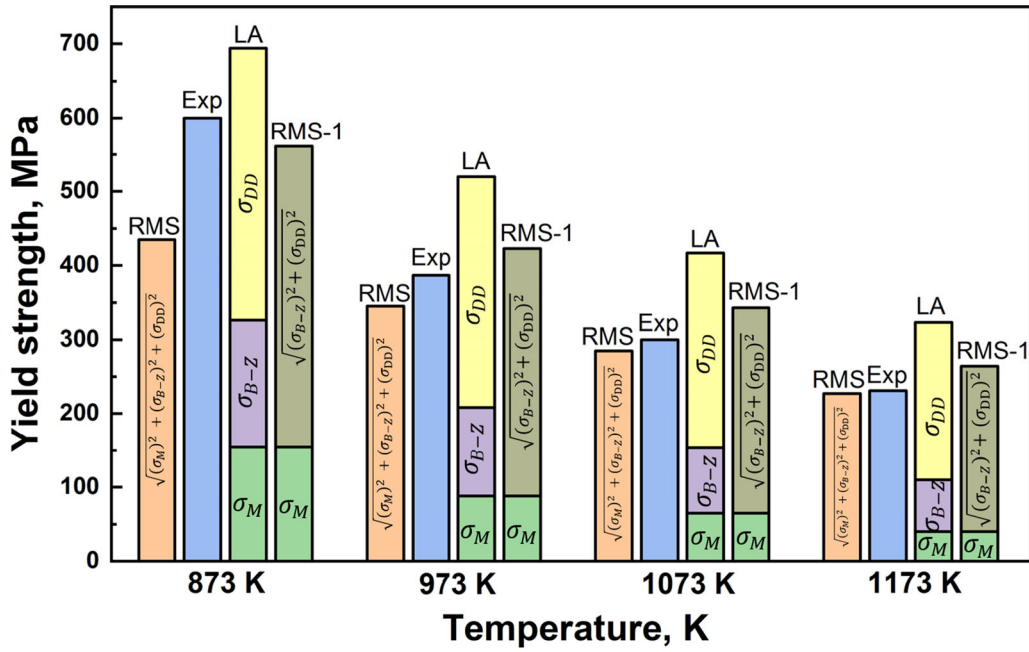
Fig. 7—Comparison of yield strength predicted using linear addition (LA) and root mean square (RMS) summation methods with experimental yield strength values in regimes II and III (873 K to 1173 K).

T_M)]),[43] b is the Burgers vector = 0.25 nm, r is the nanoprecipitate size = 2.05 nm, k_B is the Boltzmann constant, T is the absolute temperature (K), K_r is the relaxation parameter ($0 < K_r < 1$), σ_{DD} is the stress calculated from DD model (MPa), σ_d is the detachment stress (MPa), σ_{Or} is the Orowan stress (MPa) given by Eq. [5], $\dot{\varepsilon}_o$ is the reference strain rate (s^{-1}), λ is the inter-particle spacing from center to center = 36 nm, ρ is the dislocation density (5×10^{13} m^{-2}), $D_v\left(= D_{ov}exp\left(-Q_{sd}/RT\right)\right)$ is the self-diffusion coefficient. The temperature dependence of D_v was calculated by taking D_{ov} = 1.9 x 10^{-4} m^2/s and activation energy for self-diffusion of α-iron Q_{sd} = 239 kJ/mol,[69] R is the gas constant = 8.314 J/mol K, and T_M is the melting point (1787 K).

The strength obtained in regime III above 1273 K is largely due to Rösler and Arzt mechanism.[41] Therefore, the value of K_r was varied till a good fit was obtained between the experimentally measured flow stress and the DD model predictions over the experimental range of temperatures (1273 K to 1473 K). Thus, the relaxation parameter (K_r) values obtained in regime III from 1273 K to 1473 K were linearly extrapolated up to 873 K and these values were used to calculate the σ_{DD}. It varied from 0.78 to 0.81 in the temperature range of 873 K to 1173 K. More discussion on K_r values is presented in our earlier paper.[44] Earlier, Kim et al.[34] also found a similar range of values (0.75 to 0.78) in the temperature range of 873 – 1273 K in n-ODS-14Cr steel. Accordingly, the strength due to nanoprecipitates above transition temperature estimated from dislocation detachment model (Eq. [12]) is presented in Figure 7.

Once again linear addition (LA) (Eq. [15]) and root mean square (RMS) (Eqs. [16] and [17]) summation methods are used to estimate the yield strength. The comparison of experimental yield strength and predicted yield strength for regimes II and III is shown in Figure 7.

$$\text{LA-}\sigma_{y,\text{pre}} = \sigma_M + \sigma_{\text{B-Z}} + \sigma_{\text{DD}} \qquad [15]$$

$$\text{RMS-}\sigma_{y,\text{pre}} = \sqrt{\sigma_M^2 + \sigma_{\text{B-Z}}^2 + \sigma_{\text{DD}}^2} \qquad [16]$$

$$\text{RMS-1-}\sigma_{y,\text{pre}} = \sigma_M + \sqrt{\sigma_{\text{B-Z}}^2 + \sigma_{\text{DD}}^2}, \qquad [17]$$

where σ_M is matrix strength, σ_{DD} is strength obtained from DD model, and $\sigma_{\text{B-Z}}$ strength obtained from Blum–Zeng model.

The yield strength values calculated by using Eqs. ([6], [8], and [9]) and ([15] through [17]) are compared with the experimental results for regimes I, II, and III in Figure 8. The yield strength predicted using linear addition method is much higher than the experimental strength. Results estimated by RMS method are in good agreement with the experimental results. However, it would not be possible to predict the strength precisely from models due to the uncertainties of experimentally measured microstructural parameters (such as grain size and particle size) and other parameters taken from the literature. It is found that the calculated results reasonably fit with the experimental results and more importantly the models considered in the present work are able to predict the sudden decline of the yield strength above the transition temperature. It indicates that the assumed thermally activated mechanisms are responsible for the deformation in n-ODS-18Cr steel in regime II and III. Nevertheless, in these regimes, majority part of
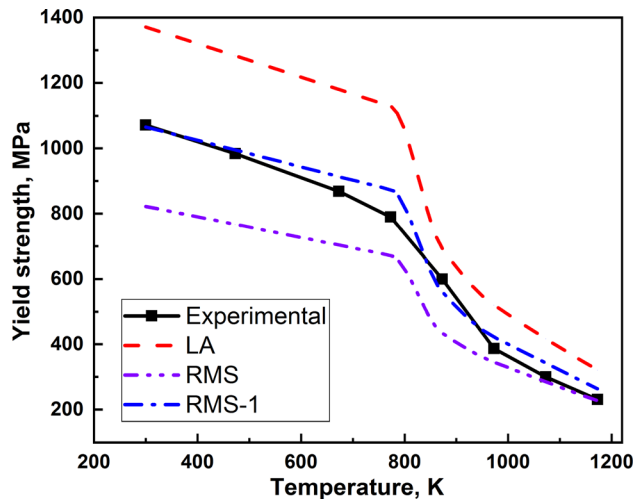
Fig. 8—Comparison of yield strength predicted using linear addition (LA) and root mean square (RMS) summation methods with experimental yield strength values in regimes I, II, and III (RT to 1173 K).

the yield strength is predominantly contributed by the dislocation detachment mechanism. Therefore, dislocation detachment mechanism would be governing the deformation at high temperatures.

IV. CONCLUSIONS

In the present work, the deformation behavior of n-ODS-18Cr ferritic steel is evaluated over a wide range of temperatures RT—1173 K and range of strain rates $10^{-4} – 10^{-2}$ s^{-1}. Three regimes are identified in the plot between the yield strength and temperature (RT to 773 K, 773 K to 973 K, and 973 K to 1173 K) indicating the change in the deformation mechanisms which govern the yield strength of n-ODS-18Cr steel in different regimes. TEM analysis reveals that the microstructure remains stable even after deformation at 1173 K and 10^{-4} s^{-1} indicating that nanoprecipitates are very stable at high temperatures and effectively pin the dislocations and grain boundaries. The models which take thermal activation into account are appropriate in predicting the yield strength behavior above the transition temperature. Nevertheless, in regimes II (773 K to 973 K) and III (973 K to 1173 K), dislocation detachment mechanism would be governing the deformation as it contributes majority part to the yield strength.

REFERENCES

1. S. Ukai, M. Harada, H. Okada, M. Inoue, S. Nomura, S. Shikakura, K. Asabe, T. Nishida, and M. Fujiwara: *J. Nucl. Mater.*, 1993, vol. 204, pp. 65–73.
2. C. Zakine, C. Prioul, and D. François: *Mater. Sci. Eng. A*, 1996, vol. 219, pp. 102–8.
3. M.J. Alinger, G.R. Odette, and G.E. Lucas: *J. Nucl. Mater.*, 2002, vol. 311, pp. 484–89.
4. R.L. Klueh, P.J. Maziasz, I.S. Kim, L. Heatherly, D.T. Hoelzer, N. Hashimoto, E.A. Kenik, and K. Miyahara: *J. Nucl. Mater.*, 2002, vols. 307–311, pp. 773–77.
5. D.T. Hoelzer, J. Bentley, M.A. Sokolov, M.K. Miller, G.R. Odette, and M.J. Alinger: *J. Nucl. Mater.*, 2007, vols. 367–370, pp. 166–72.
6. A. Hirata, T. Fujita, Y.R. Wen, J.H. Schneibel, C.T. Liu, and M.W. Chen: *Nat. Mater.*, 2011, vol. 10, pp. 922–26.
7. G. Sundararajan, R. Vijay, and A.V. Reddy: *Curr. Sci.*, 2013, vol. 105, pp. 1100-6.
8. M. Dadé, J. Malaplate, J. Garnier, F. Barcelo, F. Mompiou, P. Wident, and A. Deschamps: *Materialia*, 2018, vol. 4, pp. 585–94.
9. C.P. Massey, D.T. Hoelzer, P.D. Edmondson, A. Kini, B. Gault, K.A. Terrani, and S.J. Zinkle: *Scr. Mater.*, 2019, vol. 170, pp. 134–39.
10. J.H. Schneibel, M. Heilmaier, W. Blum, G. Hasemann, and T. Shanmugasundaram: *Acta Mater.*, 2011, vol. 59, pp. 1300–08.
11. J.H. Schneibel, C.T. Liu, M.K. Miller, M.J. Mills, P. Sarosi, M. Heilmaier, and D. Sturm: *Scr. Mater.*, 2009, vol. 61, pp. 793–96.
12. Y. Li, T. Nagasaka, T. Muroga, A. Kimura, and S. Ukai: *Fusion Eng. Des.*, 2011, vol. 86, pp. 2495–99.
13. F. Siska, L. Stratil, H. Hadraba, S. Fintova, I. Kubena, V. Hornik, R. Husak, D. Bartkova, and T. Zalezak: *Mater. Sci. Eng. A*, 2018, vol. 732, pp. 112–19.
14. S. Ukai, T. Kaito, S. Narita, T. Fujiwara, and T. Kobayashi: *ISIJ Int.*, 2003, vol. 43, pp. 2038–45.
15. S. Ukai, S. Ohtsuka, T. Kaito, H. Sakasegawa, N. Chikata, S. Hayashi, and S. Ohnuki: *Mater. Sci. Eng. A*, 2009, vols. 510–511, pp. 115–20.
16. M. Nagini, R. Vijay, M. Ramakrishna, a. V. Reddy, and G. Sundararajan: *Mater. Sci. Eng. A*, 2015, vol. 620, pp. 490–9.
17. A. Steckmeyer, M. Praud, B. Fournier, J. Malaplate, J. Garnier, J.L. Béchade, I. Tournié, A. Tancray, A. Bougault, and P. Bonnaillie: *J. Nucl. Mater.*, 2010, vol. 405, pp. 95–100.
18. M. Dadé, J. Malaplate, J. Garnier, F. De Geuser, F. Barcelo, P. Wident, and A. Deschamps: *Acta Mater.*, 2017, vol. 127, pp. 165–77.
19. J.H. Kim, T.S. Byun, and D.T. Hoelzer: *J. Nucl. Mater.*, 2010, vol. 407, pp. 143–50.
20. M. Serrano, M. Hernández-Mayoral, and A. García-Junceda: *J. Nucl. Mater.*, 2012, vol. 428, pp. 103–09.
21. S.F. Li, Z.J. Zhou, P.H. Wang, H.Y. Sun, M. Wang, and G.M. Zhang: *Mater. Des.*, 2016, vol. 90, pp. 318–29.
22. Y. de Carlan, J.-L. Bechade, P. Dubuisson, J.-L. Seran, P. Billot, A. Bougault, T. Cozzika, S. Doriot, D. Hamon, J. Henry, M. Ratti, N. Lochet, D. Nunes, P. Olier, T. Leblond, and M.H. Mathon: *J. Nucl. Mater.*, 2009, vols. 386–388, pp. 430–32.
23. A. Kimura, R. Kasada, N. Iwata, H. Kishimoto, C.H. Zhang, J. Isselin, P. Dou, J.H. Lee, N. Muthukumar, T. Okuda, M. Inoue, S. Ukai, S. Ohnuki, T. Fujisawa, and T.F. Abe: *J. Nucl. Mater.*, 2011, vol. 417, pp. 176–79.
24. S. Li, Z. Zhou, M. Li, M. Wang, and G. Zhang: *J. Alloys Compd.*, 2015, vol. 648, pp. 39–45.
25. M. Nagini, R. Vijay, and K.V. Rajulapati: *Metall. Mater. Trans. A*, 2016, vol. 47A, pp. 4197–4209.
26. Z. Oksiuta, P. Mueller, P. Spätig, and N. Baluc: *J. Nucl. Mater.*, 2011, vol. 412, pp. 221–26.
27. Q. Zhao, L. Yu, Z. Ma, H. Li, Z. Wang, and Y. Liu: *Materials*, 2018, vol. 11, p. 1044.
28. X. Boulnat, D. Fabregue, M. Perez, M.-H. Mathon, and Y. de Carlan: *Metall. Mater. Trans. A*, 2013, vol. 44A, pp. 2461–65.
29. X. Boulnat, M. Perez, D. Fabregue, T. Douillard, M.H. Mathon, and Y. De Carlan: *Metall. Mater. Trans. A.*, 2014, vol. 45A, pp. 1485–97.

30. M. Praud, F. Mompiou, J. Malaplate, D. Caillard, J. Garnier, A. Steckmeyer, and B. Fournier: *J. Nucl. Mater.*, 2012, vol. 428, pp. 90–97.
31. A. Chauhan, F. Bergner, A. Etienne, J. Aktaa, Y. de Carlan, C. Heintze, D. Litvinov, M. Hernandez-Mayoral, E. Oñorbe, B. Radiguet, and A. Ulbricht: *J. Nucl. Mater.*, 2017, vol. 495, pp. 6–19.
32. M. Nagini, R. Vijay, K.V. Rajulapati, A.V. Reddy, and G. Sundararajan: *Mater. Sci. Eng. A*, 2017, vol. 708, pp. 451–59.
33. J. Shen, Y. Li, F. Li, H. Yang, Z. Zhao, S. Kano, Y. Matsukawa, Y. Satoh, and H. Abe: *Mater. Sci. Eng. A*, 2016, vol. 673, pp. 624–32.
34. J.H. Kim, T.S. Byun, D.T. Hoelzer, C.H. Park, J.T. Yeom, and J.K. Hong: *Mater. Sci. Eng. A*, 2013, vol. 559, pp. 111–18.
35. R. Rahmanifard, H. Farhangi, A.J. Novinrooz, and S. Moniri: *Metall. Mater. Trans. A*, 2012, vol. 44A, pp. 990–98.
36. J. Ren, L. Yu, Y. Liu, C. Liu, H. Li, and J. Wu: *Materials*, 2018, vol. 11, p. 118.
37. M.C. Brandes, L. Kovarik, M.K. Miller, G.S. Daehn, and M.J. Mills: *Acta Mater.*, 2012, vol. 60, pp. 1827–39.
38. J.H. Kim, T.S. Byun, D.T. Hoelzer, S.-W. Kim, and B.H. Lee: *Mater. Sci. Eng. A*, 2013, vol. 559, pp. 101–10.
39. R. Jarugula, P.S. Babu, S.G.S. Raman, and G. Sundararajan: *Materialia*, 2020, vol. 12, p. 100788.
40. A. Chauhan, D. Litvinov, Y. de Carlan, and J. Aktaa: *Mater. Sci. Eng. A*, 2016, vol. 658, pp. 123–34.
41. J. Rösler and E. Arzt: *Acta Met. Mater.*, 1990, vol. 38, pp. 671–83.
42. S. Seils, A. Kauffmann, F. Hinrichs, D. Schliephake, T. Boll, and M. Heilmaier: *Mater. Sci. Eng. A*, 2020, vol. 786, p. 139452.
43. R. DiDomizio, S. Huang, L. Dial, J. Ilavsky, and M. Larsen: *Metall. Mater. Trans. A*, 2014, vol. 45A, pp. 5409–18.
44. R. Jarugula, S.G.S. Raman, and G. Sundararajan: *Materialia*, 2019, vol. 6, p. 100257.
45. D. Brunner and J. Diehl: *Phys. Status Solidi*, 1987, vol. 104, pp. 145–55.
46. M.M. Hutchison: *Philos. Mag.*, 1963, vol. 8, pp. 121–27.
47. C.E. Lacy and M. Gensamer: *Trans. AsM*, 1944, vol. 32, pp. 88–110.
48. G.I. Taylor: *Proc. R. Soc. Lond. A*, 1934, vol. 145, pp. 362–87.
49. B. Mouawad, X. Boulnat, D. Fabrègue, M. Perez, and Y. De Carlan: *J. Nucl. Mater.*, 2015, vol. 465, pp. 54–62.
50. J. Bentley and D. Hoelzer: *Microsc. Microanal.*, 2008, vol. 14, pp. 1416–17.
51. A. Steckmeyer, V.H. Rodrigo, J.M. Gentzbittel, V. Rabeau, and B. Fournier: *J. Nucl. Mater.*, 2012, vol. 426, pp. 182–88.
52. E.O. Hall: *Proc. Phys. Soc. Sect. B*, 1951, vol. 64, pp. 747–53.
53. J.H. Schneibel and M. Heilmaier: *Mater. Trans.*, 2015, vol. 55, pp. 44–51.
54. J.W. Martin: *Micromechanisms in Particle-Hardened Alloys*, Cambridge University Press, Cambridge, 1980.
55. U.F. Kocks, A.S. Argon, and M.F. Ashby: *Prog. Mater. Sci.*, 1975, vol. 19, pp. 1–291.
56. E. Nembach: *Acta Met. Mater.*, 1992, vol. 40, pp. 3325–30.
57. J. Lu, O. Omotoso, J.B. Wiskel, D.G. Ivey, and H. Henein: *Metall. Mater. Trans. A*, 2012, vol. 43A, pp. 3043–61.
58. J.B. Ferguson, B.F. Schultz, D. Venugopalan, H.F. Lopez, P.K. Rohatgi, K. Cho, and C.S. Kim: *Met. Mater. Int.*, 2014, vol. 20, pp. 375–88.
59. C.E. Carlton and P.J. Ferreira: *Acta Mater.*, 2007, vol. 55, pp. 3749–56.
60. W. Blum and X.H. Zeng: *Acta Mater.*, 2009, vol. 57, pp. 1966–74.
61. W. Blum and X.H. Zeng: *Acta Mater.*, 2011, vol. 59, pp. 6205–06.
62. J.H. Kim, T.S. Byun, and D.T. Hoelzer: *J. Nucl. Mater.*, 2012, vol. 425, pp. 147–55.
63. D. Srolovitz, R. Petkovic-Luton, and M.J. Luton: *Scr. Metall.*, 1982, vol. 16, pp. 1401–06.
64. E. Arzt and D.S. Wilkinson: *Acta Metall.*, 1986, vol. 34, pp. 1893–98.
65. E. Arzt and J. Rösler: *Acta Metall.*, 1988, vol. 36, pp. 1053–60.
66. Y.J. Li, X.H. Zeng, and W. Blum: *Acta Mater.*, 2004, vol. 52, pp. 5009–18.
67. W. Blum, Y.J. Li, J. Chen, X.H. Zeng, and K. Lu: *Int. J. Mater. Res.*, 2006, vol. 97, pp. 1661–66.
68. H.J. Frost and M.F. Ashby: *Deformation Mechanism Maps: The Plasticity and Creep of Metals and Ceramics*, Pergamon Press, Oxford, 1982.
69. F.S. Buffington, K. Hirano, and K. Cohen: *Acta Metall.*, 1961, vol. 9, pp. 434–39.